
















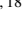















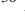


Early Results from GLASS-JWST. XIX: A High Density of Bright Galaxies at $z \approx 10$ in the Abell 2744 Region

MARCO CASTELLANO ¹, ADRIANO FONTANA ¹, TOMMASO TREU ², EMILIANO MERLIN ¹, PAOLA SANTINI ¹, PIETRO BERGAMINI ^{3,4},
CLAUDIO GRILLO ^{3,5}, PIERO ROSATI ^{6,4}, ANA ACEBRON ^{3,5}, NICHIA LEETHOCHAWALIT ⁷, DIEGO PARIS,¹ ANDREA BONCHI,⁸ DAVIDE BELFIORI,¹
ANTONELLO CALABRÒ ¹, MATTEO CORRENTI,⁸ MARIO NONINO ⁹, GIANLUCA POLENTA,⁸ MICHELE TRENTI ^{10,11}, KRISTAN BOYETT ^{10,11},
G. BRAMMER ^{12,13}, TOM BROADHURST ^{14,15,16}, GABRIEL B. CAMINHA ^{17,18}, WENLEI CHEN ¹⁹, ALEXEI V. FILIPPENKO ²⁰,
KARL GLAZEBROOK ²¹, SARA MASCIA ¹, CHARLOTTE A. MASON ^{22,23}, MASSIMO MENEGHETTI ²⁴, AMATA MERCURIO ^{25,26},
BENJAMIN METHA ^{10,11,2}, TAKAHIRO MORISHITA ²⁷, THEMIYA NANAYAKKARA ²¹, LAURA PENTERICCI ¹, GUIDO ROBERTS-BORSANI ²,
NAMRATA ROY ²⁸, EROS VANZELLA ²⁴, BENEDETTA VULCANI ²⁹, LILAN YANG ³⁰ AND XIN WANG ^{31,32,33}

¹INAF - Osservatorio Astronomico di Roma, via di Frascati 33, 00078 Monte Porzio Catone, Italy

²Department of Physics and Astronomy, University of California, Los Angeles, 430 Portola Plaza, Los Angeles, CA 90095, USA

³Dipartimento di Fisica, Università degli Studi di Milano, via Celoria 16, I-20133 Milano, Italy

⁴INAF - OAS, Osservatorio di Astrofisica e Scienza dello Spazio di Bologna, via Gobetti 93/3, I-40129 Bologna, Italy

⁵INAF—IASF Milano, via A. Corti 12, I-20133 Milano, Italy

⁶Dipartimento di Fisica e Scienze della Terra, Università degli Studi di Ferrara, Via Saragat 1, I-44122 Ferrara, Italy

⁷National Astronomical Research Institute of Thailand (NARIT), Mae Rim, Chiang Mai, 50180, Thailand

⁸Space Science Data Center, Italian Space Agency, via del Politecnico, 00133, Roma, Italy

⁹INAF - Osservatorio Astronomico di Trieste, Via Tiepolo 11, I-34131 Trieste, Italy

¹⁰School of Physics, University of Melbourne, Parkville 3010, VIC, Australia

¹¹ARC Centre of Excellence for All Sky Astrophysics in 3 Dimensions (ASTRO 3D), Australia

¹²Cosmic Dawn Center (DAWN), Denmark

¹³Niels Bohr Institute, University of Copenhagen, Jagtvej 128, DK-2200 Copenhagen N, Denmark

¹⁴Department of Theoretical Physics, University of the Basque Country UPV-EHU, 48040 Bilbao, Spain

¹⁵Donostia International Physics Center (DIPC), 20018 Donostia, The Basque Country

¹⁶IKERBASQUE, Basque Foundation for Science, Alameda Urquijo, 36-5 48008 Bilbao, Spain

¹⁷Technische Universität München, Physik-Department, James-Frank Str. 1, 85748 Garching, Germany

¹⁸Max-Planck-Institut für Astrophysik, Karl-Schwarzschild-Str. 1, D-85748 Garching, Germany

¹⁹School of Physics and Astronomy, University of Minnesota, 116 Church Street SE, Minneapolis, MN 55455, USA

²⁰Department of Astronomy, University of California, Berkeley, CA 94720-3411, USA

²¹Centre for Astrophysics and Supercomputing, Swinburne University of Technology, PO Box 218, Hawthorn, VIC 3122, Australia

²²Cosmic Dawn Center (DAWN)

²³Niels Bohr Institute, University of Copenhagen, Jagtvej 128, 2200 København N, Denmark

²⁴INAF – OAS, Osservatorio di Astrofisica e Scienza dello Spazio di Bologna, via Gobetti 93/3, I-40129 Bologna, Italy

²⁵Dipartimento di Fisica “E.R. Caianiello”, Università Degli Studi di Salerno, Via Giovanni Paolo II, I-84084 Fisciano (SA), Italy

²⁶INAF - Osservatorio Astronomico di Capodimonte, Via Moiariello 16, 80131 Napoli, Italy

²⁷IPAC, California Institute of Technology, MC 314-6, 1200 E. California Boulevard, Pasadena, CA 91125, USA

²⁸Center for Astrophysical Sciences, Department of Physics and Astronomy, The Johns Hopkins University, Baltimore, MD 21218, USA

²⁹INAF Osservatorio Astronomico di Padova, vicolo dell'Osservatorio 5, 35122 Padova, Italy

³⁰Kavli Institute for the Physics and Mathematics of the Universe, The University of Tokyo, Kashiwa, Japan 277-8583

³¹School of Astronomy and Space Science, University of Chinese Academy of Sciences (UCAS), Beijing 100049, China

³²National Astronomical Observatories, Chinese Academy of Sciences, Beijing 100101, China

³³Institute for Frontiers in Astronomy and Astrophysics, Beijing Normal University, Beijing 102206, China

ABSTRACT

We report the detection of a high density of redshift $z \approx 10$ galaxies behind the foreground cluster Abell 2744, selected from imaging data obtained recently with NIRCcam onboard *JWST* by three programs — GLASS-*JWST*, UNCOVER, and DDT#2756. To ensure robust estimates of the lensing magnification μ , we use an improved version of our model that exploits the first epoch of NIRCcam images and newly obtained MUSE

spectra, and avoids regions with $\mu > 5$ where the uncertainty may be higher. We detect seven bright $z \approx 10$ galaxies with demagnified rest-frame $-22 \lesssim M_{UV} \lesssim -19$ mag, over an area of ~ 37 sq. arcmin. Taking into account photometric incompleteness and the effects of lensing on luminosity and cosmological volume, we find that the density of $z \approx 10$ galaxies in the field is about $10\times$ ($3\times$) larger than the average at $M_{UV} \approx -21(-20)$ mag reported so far. The density is even higher when considering only the GLASS-JWST data, which are the deepest and the least affected by magnification and incompleteness. The GLASS-JWST field contains 5 out of 7 galaxies, distributed along an apparent filamentary structure of 2 Mpc in projected length, and includes a close pair of candidates with $M_{UV} < -20$ mag having a projected separation of only 16 kpc. These findings suggest the presence of a $z \approx 10$ overdensity in the field. In addition to providing excellent targets for efficient spectroscopic follow-up observations, our study confirms the high density of bright galaxies observed in early *JWST* observations, but calls for multiple surveys along independent lines of sight to achieve an unbiased estimate of their average density and a first estimate of their clustering.

Keywords: Lyman-break galaxies — Reionization — Surveys

1. INTRODUCTION

In just a few months, *JWST* has started to transform our understanding of the epoch of “cosmic dawn,” when the first sources of light likely started reionizing the intergalactic medium (Dayal & Ferrara 2018; Robertson 2022). Previous *Hubble Space Telescope* (*HST*) and ground-based surveys were mostly limited to exploring galaxies at redshift $z \approx 6-8$, about 1 Gyr after the Big Bang (e.g., Finkelstein et al. 2015; Castellano et al. 2016; Bouwens et al. 2021), and only yielded small samples of bright galaxies at $z \gtrsim 9$ (e.g., McLeod et al. 2016; Oesch et al. 2018; Morishita et al. 2018; Bowler et al. 2020; Roberts-Borsani et al. 2022a; Leethochawalit et al. 2022a; Bagley et al. 2022). The public datasets gathered through the *JWST* Early Release Observations (Pontoppidan et al. 2022) and Early Release Science Programs have enabled the detection of tens of candidate sources at $z > 9$, pushing the cosmic frontier to the first 200–300 Myr after the Big Bang (e.g., Castellano et al. 2022a; Donnan et al. 2022; Finkelstein et al. 2022a; Morishita & Stiavelli 2022; Naidu et al. 2022; Yan et al. 2022; Roberts-Borsani et al. 2022b; Robertson et al. 2022).

The results have been surprising: multiple independent analyses have shown that the number density of bright galaxies at $z > 9$ is larger than predicted by theoretical models or on the basis of the extrapolation from lower-redshift estimates (e.g., Finkelstein et al. 2022b; Harikane et al. 2022; Bouwens et al. 2022b; Mason et al. 2022; Ferrara et al. 2022).

This excess is most pronounced in the brightest part of the luminosity function (LF), which seems to evolve very little from $z = 4$ to $z = 10-12$. This result is particularly tantalizing, because the brightest objects are detected at high significance in multiple bands and display a deep break, and are thus unlikely to be significantly contaminated by low-redshift interlopers (e.g., Fujimoto et al. 2022).

The origin of this excess is still to be determined — it can be either due to a higher efficiency in star formation and

galaxy assembly than previously thought, which makes them more abundant and/or massive, or to deviations from common prior assumptions on their physical properties (e.g., the initial mass function, IMF, and/or the metallicity and/or dust content) that increase their flux (Mason et al. 2022; Kohandel et al. 2022; Ziparo et al. 2022; Fiore et al. 2022). More extreme explanations refer to non-standard cosmologies to increase the abundance of bright and/or massive objects at very high redshift (e.g., Melia 2014; Boylan-Kolchin 2022; Menci et al. 2022; Kannan et al. 2022).

Among the various fields targeted by early *JWST* surveys, the first observations of a flanking field to the Abell 2744 (A2744 hereafter) cluster within the GLASS-JWST project delivered two of the brightest candidates at $z > 10$, dubbed GHZ1/GLASSz10 (at $z \approx 10.5$) and GHZ2/GLASSz12 (at $z \approx 12.3$) respectively (Castellano et al. 2022a, C22a hereafter, Naidu et al. 2022; Bakx et al. 2022; Donnan et al. 2022; Harikane et al. 2022; Yoon et al. 2022). Compared to other detections (or lack of) in other and often larger fields, the GLASS-JWST field immediately qualified itself as one of the most interesting areas to investigate the most luminous sources at cosmic dawn.

Recently, more data have been obtained on the A2744 area by a number of *JWST* programs: the second epoch of the GLASS-JWST Early Release Science Program (Treu et al. 2022, JWST-ERS-1324), the UNCOVER program (PIs Labbé and Bezanson, JWST-GO#2561 Bezanson et al. 2022), and the DDT program #2756 (PI Wenlei Chen), which significantly extend and deepen the surveyed area. We take advantage of these new data and present here the analysis of the abundance of galaxies at $z \approx 9-11$ selected in the NIR-Cam imaging data in the entire A2744 region, with two goals: (i) improve the determination of the density of bright galaxies at $z \approx 10$, and (ii) start to characterize the clustering properties of this population.

Table 1. NIRCam imaging

Filter	GLASS-JWST	DDT	UNCOVER
F090W	29.5	-	-
F115W	29.7	28.2	29.1
F150W	29.5	28.3	29.0
F200W	29.6	28.6	29.0
F277W	29.8	28.8	29.3
F356W	29.9	28.8	29.4
F410M	-	-	28.8
F444W	29.6	28.6	28.9

NOTE— 5σ depths for point sources within a circular aperture of diameter $0''.2$.

Throughout the paper we adopt AB magnitudes (Oke & Gunn 1983), a Chabrier (2003) IMF, and a flat Λ -CDM concordance model ($H_0 = 70.0 \text{ km s}^{-1} \text{ Mpc}^{-1}$, $\Omega_M = 0.30$).

2. NIRCAM IMAGING AND PHOTOMETRY

The NIRcam data analyzed in this paper are taken from three programs focused on the cluster A2744 and its surroundings. The GLASS-JWST NIRCam images have been taken in parallel to NIRISS on June 28–29 2022, and in parallel to NIRSpec on Nov. 10–11, 2022. They consist of imaging through seven broad-band filters spanning from F090W to F444W as described by Treu et al. (2022). The UNCOVER NIRCam observations of the cluster A2744 were taken on November 2–4–7 and 15, and exploit the same filter set as GLASS-JWST, except that the F090W filter is replaced by F410M. Finally, NIRCAM imaging of A2744 was obtained as part of DDT program 2756 on October 20. The DDT-2756 (DDT hereafter) filter set is the same as GLASS-JWST with the exception of the F090W filter, and overall shorter exposure times. The pointings overlap partially, resulting in the field geometry illustrated in Figure 1 (top). The image reduction, and the methods used to detect sources and measure multiband photometry, build on those described by Merlin et al. (2022), and take into account the improvements in data processing and calibration that have become available since then. A detailed description is given in a companion paper by Paris et al. (in prep.). For convenience of the reader, we briefly summarize below the information relevant for the present paper. Data reduction and flux calibration were obtained using the official *JWST* pipeline¹ and exploiting the calibration files *JWST_1019.PMAP* made available by

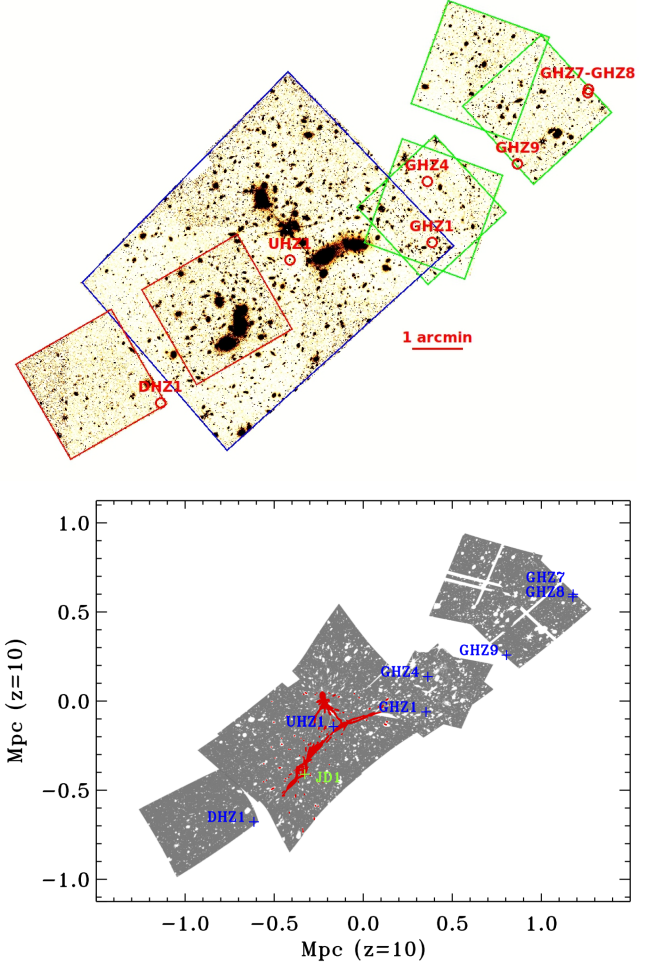


Figure 1. **Top:** layout of the field and position of the $z \approx 10$ candidates (red circles). The F444W mosaic combines observations from GLASS-JWST ERS (green region), UNCOVER (blue), and DDT-2756 (red). **Bottom:** the source plane at $z = 10$. Masked regions outside the mosaics or covered by foreground objects are shown in white. The red region is the area with $\mu > 5$ not used to compute the UV LF in the present paper; the triply lensed source JD1 at $z_{\text{spec}} = 9.79$ (green cross) lies in this region and is not included in our sample.

STScI in November 2022. We have then used a pipeline already adopted in similar projects (Fontana et al. 2014) and based on SCAMP (Bertin 2006) and SWARP (Bertin et al. 2002) to combine the single exposures into mosaics projected onto a common grid of pixels. For simplicity, considering the different depth and filter coverage of the three programs, and the need to perform simulations to assess the incompleteness in color space, we analyzed the three datasets independently and performed the simulations on each dataset separately. To avoid double counting, certain regions have been excluded from a given dataset when deeper exposures exist in another one: in practice, we have removed the UNCOVER NW cor-

¹ <https://jwst-docs.stsci.edu/jwst-science-calibration-pipeline-overview>

ner (observed by GLASS-JWST) and the portion of the DDT pointing that overlaps with UNCOVER.

Objects were detected using a customized version of SExtractor (Bertin & Arnouts 1996; Guo et al. 2013, v2.8.6) on the F444W coadded images. Total F444W fluxes in elliptical apertures as defined by Kron (1980) were measured with A-PHOT (Merlin et al. 2019). Fluxes in the other bands were measured with A-PHOT in several apertures at the positions of the detected sources using images point-spread-function (PSF)-matched to the F444W one. In the present analysis we use fluxes obtained by scaling the total F444W flux on the basis of the relevant color in $2 \times \text{FWHM}$ diameter ($= 0''.28$) apertures. The mosaics are a combination of different exposures resulting in non-uniform depths. We summarize in Table 1 the typical 5σ depths of the deepest regions for point sources within a circular aperture of diameter $0''.2$. Less exposed regions can be 0.2–0.3 mags shallower depending on the band and field.

We estimate total areas of 22.5, 10.2 and 4.6 sq. arcmin in the UNCOVER, GLASS-JWST, and DDT fields, respectively, available for the selection of high-redshift candidates by considering the regions observed in all bands, and excluding the pixels occupied by foreground sources.

3. SELECTED GALAXIES AT $Z \approx 10$

We select objects at $z \approx 9$ –11.5 using the color-color selection window defined by C22a:

$$\begin{aligned} (F115W - F150W) &> 1.7 \\ (F115W - F150W) &> 2.17 \times (F200W - F277W) + 1.7 \\ -0.8 &< (F200W - F270W) < 0.6. \end{aligned}$$

We require signal-to-noise ratio (SNR) > 8 in the F444W band, SNR > 2 in the other bands redward of the Lyman break, and SNR < 2.0 in the F090W band, where available. The selection yields 5 candidates in the GLASS-JWST field, 2 in UNCOVER, and 1 in the DDT region.

The five selected objects in GLASS-JWST include GHZ1 and GHZ4 from C22a, and three galaxies in the region recently observed in the NIRSpec parallel and discussed here for the first time. In UNCOVER we reselect object JD1B from Zitrin et al. (2014) recently confirmed to be at $z = 9.76$ with NIRSpec (Roberts-Borsani et al. 2022b), and a new robust candidate UHZ1 with $m_{F444W} = 26.54 \pm 0.09$ mag, outside of the area previously observed by the HFF. We will not discuss further object JD1B which is one of the multiple images of a strongly magnified ultra-faint galaxy and will not be used to estimate the UV LF in the present analysis which is limited to moderate magnification regions (see Sect. 4). We checked the other counter-images reported by Zitrin et al.

(2014) finding that JD1A is not selected because it is just outside the color selection region, while the faintest one, JD1C, is not detected likely due to the strong background in the F444W band from a nearby cluster galaxy. The only candidate selected in the DDT program is also the brightest in the sample, with $m_{F444W} = 24.82 \pm 0.05$ mag.

Objects GHZ1, GHZ4, and GHZ9 (from GLASS-JWST), and the UNCOVER and DDT candidates, have also been observed with *HST* under the HFF and BUFFALO (Steinhardt et al. 2020) programs. We further assessed their reliability by measuring the SNR at their position in the F606W, F814W, and F105W mosaics processed with the *grizli* pipeline (Brammer 2022) in $0''.2$ diameter apertures, finding SNR < 2 in all cases.

For all selected candidates we estimate photometric redshifts with EAZY (Brammer et al. 2008) and ZPHOT (Fontana et al. 2000). The EAZY code was run assuming a flat prior with two different sets of templates: the default V1.3 spectral template (see Leethochawalit et al. 2022b), and the recently released templates by Larson et al. (2022) specifically designed for the analysis of *JWST*-selected galaxies at very high redshift. The analysis with ZPHOT has been performed as described by Santini et al. (2022) by fitting the observed photometry with Bruzual & Charlot (2003, BC03 hereafter) templates having both declining and delayed star-formation histories and models the contribution from nebular continuum and line emission following Schaerer & de Barros (2009) and Castellano et al. (2014). We show spectral energy distributions (SEDs), photometric redshift probability distributions, and thumbnails of the seven candidates in Figs. 2 and 3. Their properties are listed in Table 2, including demagnified M_{UV} and μ values based on the lensing model that will be discussed in Sect. ???. The two objects GHZ1 and GHZ4 from C22a fall in the region recently reobserved in parallel to NIRSpec. Reassuringly, their SEDs and photometric redshifts obtained from the new data are in excellent agreement with those measured on the first GLASS-JWST NIRCам observations, with the deeper data analyzed here reducing the likelihood of the secondary photometric redshift solution at $z \approx 2$ for GHZ4. The availability of the lensing model extending to the GLASS-JWST region allows us to estimate that they are moderately magnified, such that the intrinsic M_{UV} are ~ 0.5 – 0.6 mag fainter than the estimates reported in our previous paper. The three newly found candidates in the newly observed GLASS-JWST area have observed $m_{F444W} \approx 27$ – 27.3 mag and similar SEDs. Two of them (GHZ7 and GHZ8, see Fig. 1) have very similar $P(z)$ and are separated by only $4''$ on the sky, corresponding to a projected separation of 16 kpc at $z \sim 10$ — i.e. they are likely to be physically associated in a close pair. Two of the other three candidates previously reported by C22a (GHZ5 and GHZ6) do not enter the present sample as with the new photometry they are located just out-

Table 2. Galaxy Candidates at $z = 9$ –11 in the GLASS-JWST, DDT, and UNCOVER fields

ID	R.A.	Dec	F200W	F444W	M_{UV}	z_{phot}	$z_{EAzY-v1p3}$	$z_{EAzY-Larson}$	μ
	deg.	deg.	AB mag	AB mag					
GHZ1	3.511929	-30.371859	26.66 \pm 0.03	26.28 \pm 0.04	-20.38 $^{+0.31}_{-0.19}$	10.47	10.39	10.54	1.69 $^{+0.23}_{-0.56}$
GHZ4	3.513739	-30.351561	27.61 \pm 0.17	27.35 \pm 0.08	-19.47 $^{+0.16}_{-0.26}$	10.27	10.11	10.43	1.63 $^{+0.16}_{-0.14}$
GHZ7	3.451363	-30.320718	27.44 \pm 0.06	27.75 \pm 0.13	-20.08 $^{+0.02}_{-0.17}$	10.62	9.97	10.57	1.18 $^{+0.02}_{-0.02}$
GHZ8	3.451430	-30.321796	26.78 \pm 0.06	27.07 \pm 0.10	-20.75 $^{+0.02}_{-0.17}$	10.85	10.14	10.79	1.18 $^{+0.02}_{-0.02}$
GHZ9	3.478756	-30.345520	27.55 \pm 0.07	27.37 \pm 0.10	-19.36 $^{+0.04}_{-0.12}$	9.35	9.48	9.40	1.30 $^{+0.05}_{-0.04}$
DHZ1	3.617257	-30.425565	24.77 \pm 0.03	24.82 \pm 0.05	-22.14 $^{+0.03}_{-0.07}$	9.45	9.96	9.60	1.66 $^{+0.04}_{-0.04}$
UHZ1	3.567065	-30.377857	26.39 \pm 0.08	26.54 \pm 0.09	-19.77 $^{+0.16}_{-0.17}$	10.32	9.88	9.99	3.81 $^{+0.41}_{-0.56}$

NOTE—The F200W and F444W magnitudes are not corrected for magnification. The demagnified, rest-frame M_{UV} have been obtained at the best-fit z_{phot} redshift, and the uncertainties include the contribution of both photometry and magnification. The uncertainties on the magnification μ are at 95% c.l.; see Sect. ??.

side the color selection region. Their photometric redshift solutions still show a significant peak at $z > 9$ as reported by C22a, but they are not included in the present analysis which is based only on color-selected candidates. A third candidate (GHZ3) of the C22a paper is instead detected in the new and deeper images obtained in the F090W filter and it is therefore definitely not a $z \approx 10$ galaxy. Candidates GHZ1 falls also on the UNCOVER area that we have removed to avoid duplications. We note that various candidates are found not far from the image edges. However, they all fall in full-depth regions of the mosaics and we made sure that their detection and photometry is not affected by border effects. The most remarkable object in the present sample is candidate DHZ1 from the DDT area, which has a demagnified $M_{UV} = -22.1$ mag and a robust photometric redshift solution at $z \approx 9.5$ –10 with single-peaked $P(z)$.

Basic physical properties of the sample galaxies are summarized in Table 3. Corrected for lensing magnification, the star formation rates (SFR) range between 2 and 37 M_{\odot}/yr , the estimated stellar masses range between $4 \times 10^7 - 1.45 \times 10^9 M_{\odot}$, and the UV slopes β range between -1.9 and -2.7. We note that at $z \geq 10$ the rest-frame optical bands are poorly constrained by NIRCAM data, at best in regions that can be contaminated by emission lines. As a result stellar masses can be subject to uncertainties and biases, and stellar ages are poorly constrained. For this reason we do not quote the latter ones in Table 3. The reported values appear to encompass the range of rest-frame properties of Lyman-break galaxies at these redshifts, as observed by recent surveys. We report these values to facilitate follow-up and we defer a more detailed analysis of the properties of these galaxies to future work.

4. METHODOLOGY

Table 3. Physical Properties of the $z = 9$ –11 galaxy candidates

ID	SFR	M_{star}	UV slope
	$M_{\odot} \text{ yr}^{-1}$	$10^8 M_{\odot}$	
GHZ1	10.8 $^{+50.3}_{-6.1}$	11.7 $^{+9.6}_{-10.7}$	-1.93 \pm 0.07
GHZ4	2.0 $^{+15.7}_{-0.5}$	4.4 $^{+2.0}_{-4.0}$	-2.31 \pm 0.36
GHZ7	3.3 $^{+10.3}_{-0.5}$	2.1 $^{+1.9}_{-1.7}$	-2.66 \pm 0.15
GHZ8	17.8 $^{+14.1}_{-12.6}$	0.8 $^{+6.6}_{-0.16}$	-2.60 \pm 0.14
GHZ9	14.7 $^{+16.1}_{-7.56}$	3.4 $^{+3.1}_{-2.5}$	-1.92 \pm 0.13
DHZ1	37.2 $^{+73.8}_{-14.4}$	14.5 $^{+11.9}_{-6.7}$	-2.16 \pm 0.07
UHZ1	4.4 $^{+3.2}_{-2.3}$	0.4 $^{+1.9}_{-0.2}$	-2.72 \pm 0.15

NOTE—Stellar masses and SFR have been obtained at the best-fit z_{phot} redshift as in [Santini et al. \(2022\)](#) and corrected for magnification. Uncertainties include error contribution from SED-fitting and magnification. The UV slope β is measured by fitting the F200W, F277W and F356W bands, the uncertainties in the fit account for photometric errors ([Castellano et al. 2012](#)).

Estimating the luminosity function (LF) of high-redshift galaxies in lensed fields is more complex than in blank fields. The additional complexity is usually justified by the extra gain in depth afforded by lensing magnification. In this work, however, motivated by the discovery of a significant number of bright $z \approx 10$ galaxies, we focus primarily on the bright end of the LF, and postpone the study of the faintest objects to a future work. This choice allows us to keep the analysis simple and robust, building on the ingredients that we discuss below.

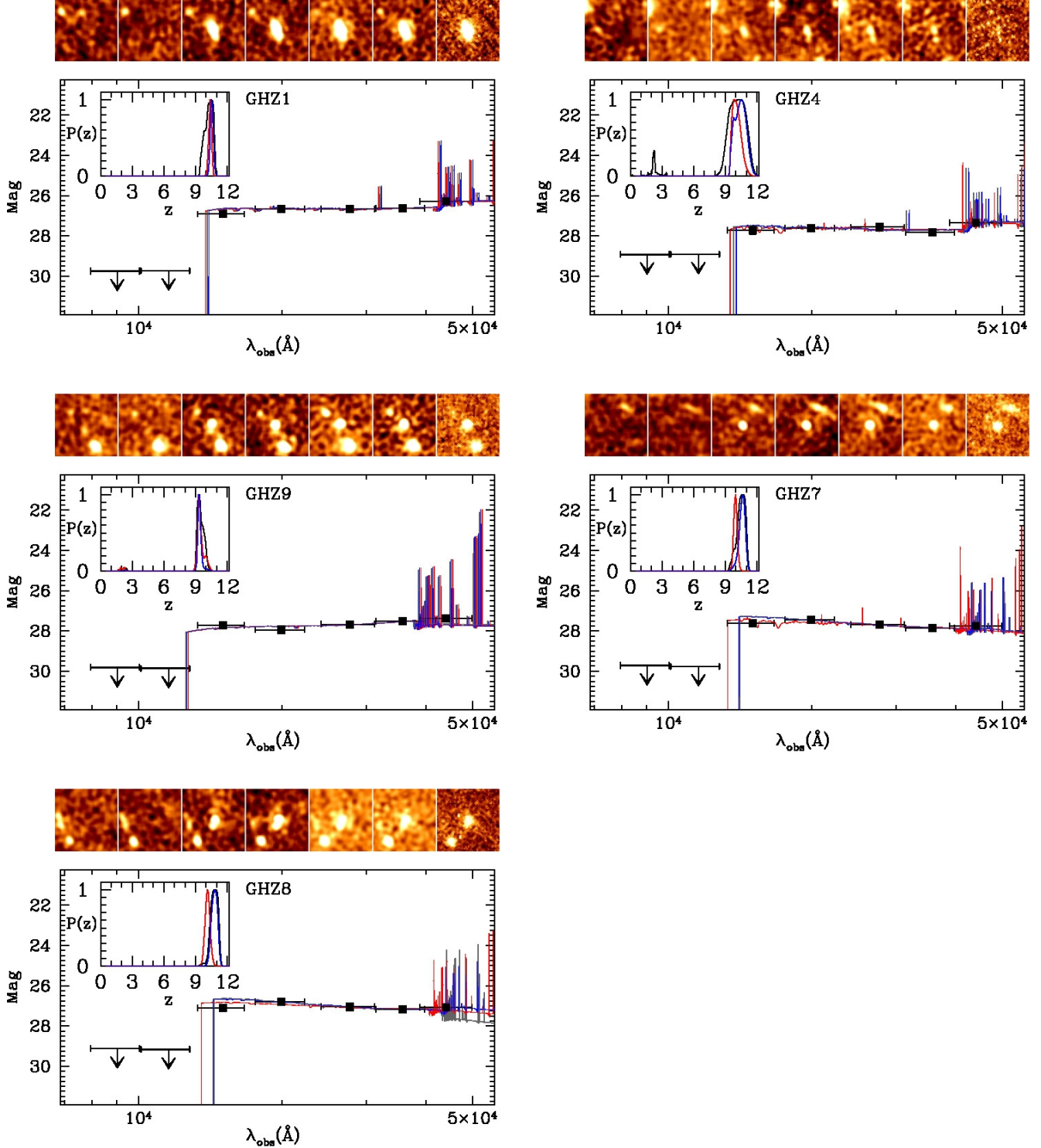


Figure 2. The $z \approx 10$ candidates from the GLASS-JWST field. Photometry (not corrected for magnification) and SEDs are given in the main quadrant. Upper limits are reported at the 2σ level. We show in the inset the redshift probability distributions $P(z)$ from z_{PHOT} (gray) and EAZY (red for the standard V1.3 templates, and blue for the Larson et al. 2022 templates). The SEDs are obtained by fitting the BC03 library described in Sect. 3 at the best-fit redshifts from the relevant z_{PHOT} and EAZY runs. Thumbnails, from left to right, show the objects in the F090W, F115W, F150W, F200W, F277W, F356W, and F444W bands.

4.1. Lens Model

The A2744 region, especially that covered by the UNCOVER data, is affected by moderate to strong lensing am-

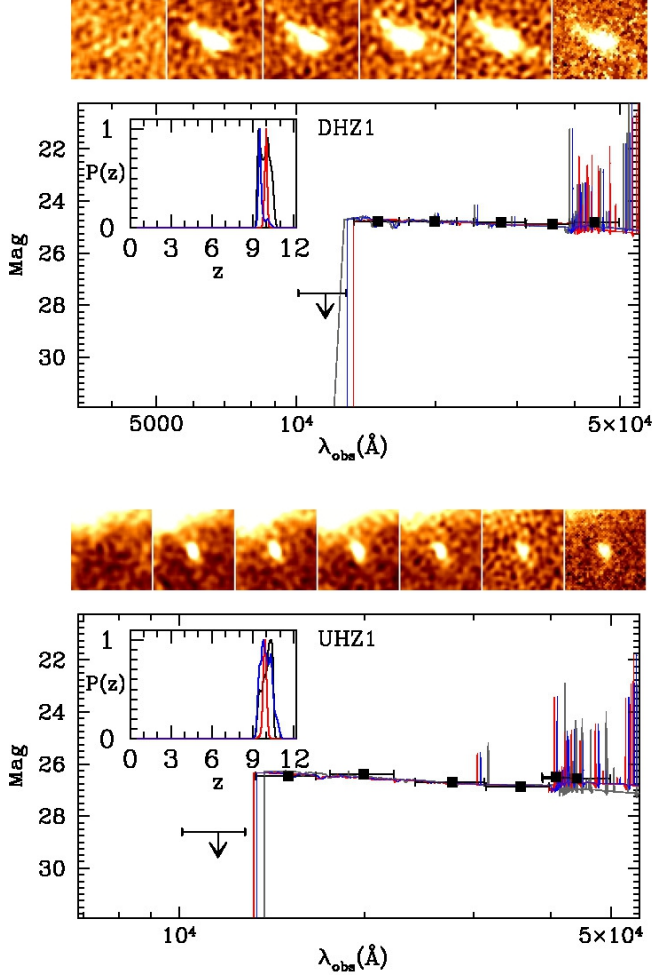


Figure 3. Same as Fig. 2 for the $z \approx 10$ candidates in the DDT field and in the low-magnification area of the UNCOVER field. Thumbnails, from left to right, show the objects in the F115W, F150W, F200W, F277W, F356W, F410M (UHZ1 only), and F444W bands.

plication due to the foreground cluster, whose mass distribution is known to extend over a wide area covering the entire dataset (e.g., Merten et al. 2011). To properly account for the lensing effect, we have extended the pre-*JWST* lens model described by Bergamini et al. (2022, B22 hereafter) by including 28 additional multiple images in the cluster core, as well as in the NW region where two cluster galaxies (named G1 and G2 by B22) are present with luminosities similar to those of the central bright cluster galaxies. Owing to the rich strong-lensing (SL) features revealed by the NIRCcam data, we refer to this region as SL clump. The identification of extra multiple images takes advantage of NIRCcam multiband photometry, as well as new spectroscopic observations with VLT/MUSE (Prieto-Lyon et al. 2022, Caminha et al. 2022, in prep.). MUSE coverage of the SL clump also enables the identification of additional cluster galaxies and the de-

termination of the velocity dispersions of G1 and G2, which are used as priors when modeling the associated subhalos, thus improving the B22 total mass reconstruction in this area. The total root-mean-square (rms) separation between the observed and model-predicted positions of the multiple images is $\sim 0''.4$, similar to that of the B22 model. A publication describing the extended and enhanced SL model is in preparation.

For the purpose of the present work, we have computed the median magnification values and 95% confidence level intervals for each high- z candidate by extracting 100 random sets of parameter values from the final MCMC chain, containing a total of 3×10^4 samples. To account for systematic uncertainties owing to the choice of the total mass parametrization in the external region, we have combined the MCMC chains of two extended lens models, which include either one or two cluster-scale halos in the SL clump, using the same set of multiple image constraints.

To derive the LF of the high- z candidates, unlensed survey areas and volumes in the considered redshift bins are needed. Intrinsic survey areas are computed for each of the three fields by projecting the footprints of the observed regions on the source plane, at varying redshift in the range $9.0 < z < 11.5$. To this aim, we use the deflection field from the extended lens model with the best positional rms uncertainty (i.e. the one including only a single halo in the SL clump region). We also project onto the source plane the observed mask (excluding regions around bright sources) and the magnification maps in the aforementioned redshift range (see Figure 1-bottom). In this way, we can reconstruct the effective area on the source plane, for each of the three fields separately, where objects can potentially be identified around $z = 10$, and compute the corresponding magnification in each pixel. These maps are then combined to estimate the probed survey volume in each redshift and luminosity bin.

The seven galaxies at $z \approx 10$ listed in Table 2 have low-to-moderate magnifications, ranging from 1.2 to ~ 4 (see Table 2), and are not multiply imaged (i.e., they lie outside the main caustics on the source plane at $z \approx 10$). This allows us to limit our LF analysis to regions with $\mu < 5$, which has the significant advantage of avoiding strongly lensed regions where systematic uncertainties can be large, albeit associated to small survey volumes. As previously mentioned, JD1B is the only object at $\mu > 5$ meeting our color-selection criteria and is thus excluded from the sample analyzed in this paper. The corresponding areas with $\mu < 5$ in the source plane amount to 7.6, 10.2 and 3.4 sq. arcmin in the GLASS-*JWST*, UNCOVER and DDT fields, respectively. By comparing the effective source plane area predicted by lens models with slightly different mass parametrization, but similar positional rms scatter, we estimate the systematic uncertainty on the ef-

Table 4. Binned Luminosity Function

M_{UV}	N_{obj}	ϕ
		$10^{-5} \text{ Mpc}^{-3} \text{ mag}^{-1}$
-22.5 ± 0.5	1	$1.6^{+5.4}_{-0.3}$
-21.0 ± 1.0	3	$3.2^{+6.3}_{-1.4}$
-19.5 ± 0.5	3	$17.8^{+35.1}_{-8.1}$

NOTE—The binned volume densities in the GLASS-JWST, UNCOVER, and DDT fields; uncertainties are computed for small-number Poisson statistics following [Gehrels \(1986\)](#).

fective survey volume (and therefore on the data points in the LF) to be approximately 5%.

We have also checked the predicted magnification values for our objects by the SL model recently released by the UNCOVER collaboration ([Furtak et al. 2022](#))². Four of our seven candidates have magnification values at $z \approx 10$ lower than 5 and in good agreement with the ones presented here, while the remaining three (i.e., GHZ7, GHZ8, and GHZ9) are not covered by their model.

4.2. Image Simulations

The choice of limiting the analysis to galaxies identified in low-magnification areas simplifies also the estimate of the completeness. We first perform a set of imaging simulations as described in C22a. The simulations are performed separately for the GLASS-JWST, UNCOVER, and DDT fields. Briefly, we inserted in blank regions of the observed images 3×10^5 mock Lyman-break galaxies (LBGs) at $9 < z < 12$ and with a uniform distribution at $-18.5 < M_{UV} < -23$ mag. The observed magnitudes are obtained by randomly associating a model from a library based on BC03 models with metallicity $Z = 0.02 Z_{\odot}$, $0 < E(B - V) < 0.2$ mag, constant star-formation history, [Salpeter \(1955\)](#) IMF, and [Calzetti et al. \(2000\)](#) extinction law. We assume that objects follow a circular [Sersic \(1968\)](#) light profile with index $n = 1$ and that their effective radius scales with L_{UV} as $r_e \propto L^{0.5}$, consistent with several estimates at comparable redshifts (e.g., [Grazian et al. 2012](#); [Kawamata et al. 2018](#); [Bouwens et al. 2022a](#); [Yang et al. 2022](#)). Following [Yang et al. \(2022\)](#), we assume an effective radius of 0.8 kpc for objects with $M_{UV} = -21$ mag. In order to avoid overcrowding, simulations are repeated by inserting 500 objects each time. Detection, photometry and color selection on the simulated galaxies are performed in the same way as for the real catalogs.

² Magnification maps made public as of Dec 12th 2022

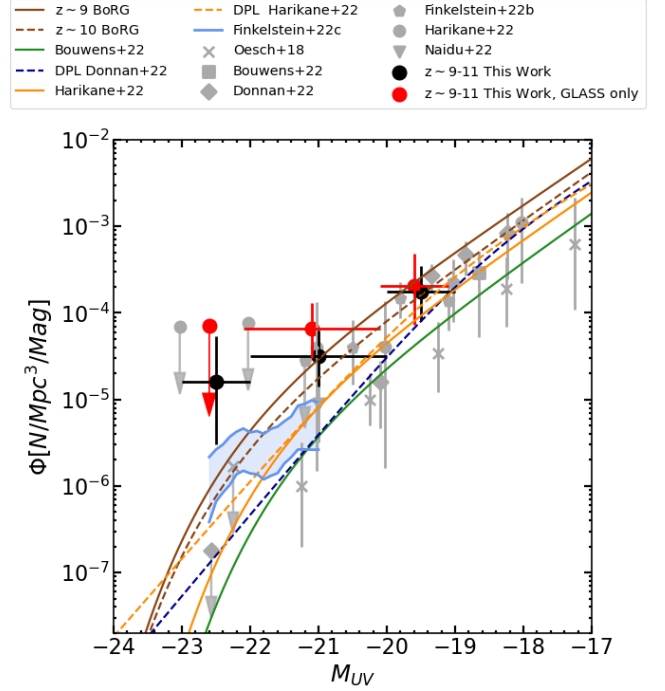


Figure 4. The UV LF at $z \approx 10$ in the A2744 region observed by the GLASS-JWST, UNCOVER, and DDT#2756 programs. Black circles and error bars are obtained from the full sample, red ones (shifted by 0.1 mag for clarity) for the GLASS-JWST field only. The uncertainties are given by small-number Poisson statistics in each bin following [Gehrels \(1986\)](#). Binned LFs from the literature are shown as gray symbols (see label for details). The shaded blue region indicate the constraints by [Finkelstein et al. \(2022c\)](#) from HST-CANDELS. We also show the LF analytic fits estimated by [Leethochawalit et al. \(2022a\)](#), BoRG survey $z \approx 9-10$, [Bouwens et al. \(2022b\)](#), [Donnan et al. \(2022\)](#), and [Harikane et al. \(2022\)](#).

5. THE $Z \approx 10$ UV LUMINOSITY FUNCTION IN THE A2744 REGION

Even correcting for magnifications, our sample has remarkably bright UV magnitudes $M_{UV} \lesssim -20$, corresponding to a high surface density of objects. We quantify the volume density by computing the UV LF in three rest-frame magnitude bins. The choice of the magnitude intervals results from a tradeoff between the best possible sampling of the luminosity distribution and the number of sources available. The effective volumes in each bin are obtained by taking into account the area at different magnification levels, and the relevant completeness for the selection of objects with the considered UV rest-frame magnitudes. In fact, the volume accessible for sources of a given *intrinsic* magnitude $M_{UV,int}$ is

$$V_{\text{eff}, M_{UV,int}} = \int_{z=9}^{z=12} \int_{\mu=1}^{\mu=5} C(M_{UV,obs}, z) \frac{dV(\mu, z)}{dz} d\mu dz, \quad (1)$$

where $M_{\text{UV,obs}} = M_{\text{UV,int}} - 2.5 \log(\mu)$. In practice, the effective volumes are calculated for the three bins reported in Table 4 by replacing the integral with sums in steps of $\Delta\mu = 0.25$ and $\Delta z = 0.25$. The completeness values C at different redshifts and magnifications are obtained on the basis of the imaging simulations described above, and the element volumes $dV(\mu, z)$ available for the selection of high-redshift galaxies are computed as a function of μ on the basis of the area of the masked magnification maps. We consider for each object the demagnified M_{UV} reported in Table 2 which has been computed on the basis of the best-fit *zPHOT* template. Considering the width of the magnitude bins, magnification and redshift uncertainties do not significantly affect our results. The binned volume densities are then obtained as $\phi_i = N_i/V_{\text{eff},i}$, where N_i is the number of objects in the considered bin. We explicitly note that the completeness C is higher than 90% in the GLASS-JWST field — the deepest of the three — while it is ~ 50 –80% in DDT and UNCOVER, because of shallower depths and, in the case of UNCOVER, crowding.

The binned UV LF is shown in Fig. 4, together with results from recent surveys in the same redshift range. The relevant values are presented in Table 4. We compute and plot in Fig. 4 the LF derived for the entire sample and considering GLASS-JWST only.

It is immediately clear that the density of $z \approx 10$ sources in our sample is significantly larger than the best-fit LF derived from previous *JWST* surveys — which in most cases include the first epoch of the GLASS-JWST data, and so may already be biased high. Our inferred density is higher also than that inferred by previous wide field imaging surveys with HST, such as BORG (Leethochawalit et al. 2022a; Bagley et al. 2022), that do not include the GLASS-JWST data and were selected with a different filter complement. The discrepancy is particularly remarkable at $M_{\text{UV}} \approx -21$, where it ranges between 4 and 10 times with respect to previous estimates, although of course there is considerable uncertainty at this stage. On the basis of the number of objects and on the surveyed volume we estimate a cosmic variance at the level of ~ 13 –15%³ in each of the three fields, where the highest value refers to the DDT region. This is much smaller than Poisson uncertainty in the number counts.

We find an even higher density if we restrict the analysis to the GLASS-JWST field (red points in Fig. 4). This is the deepest area considered, and the region least affected by magnification ($\mu \approx 1.2$ –1.7), so it is difficult to attribute this result to a higher contamination. We thus suggest that the GLASS-JWST area is likely to correspond to an overden-

sity. The sources appear aligned along a filament-like structure of projected length approximately 2 Mpc with the pair GHZ7-GHZ8, separated by 16 kpc. All galaxies have very similar colors and $P(z)$, resembling similar galaxy associations found in other high-redshift structures (e.g., Castellano et al. 2018, 2022b). The sample size is too small to carry out a meaningful study of the two-point correlation function, but determining the clustering properties of bright galaxies at $z \approx 10$ will be important to determine their average cosmic density, their halo mass, and their role in cosmic reionization (Endsley et al. 2020).

6. SUMMARY AND CONCLUSIONS

The rapid discovery of an unexpectedly large number of galaxies at $z \approx 10$ and beyond is one of the most tantalizing results obtained by the very first *JWST* observations. The higher than expected normalization of the UV LF at $z > 9$ (e.g., C22a, Finkelstein et al. 2022b) has already generated a lively theoretical debate about its potential physical explanations (e.g., Mason et al. 2022; Ferrara et al. 2022). In this context, it is important to carry out further studies to improve the statistics and start to explore the all-important issues of clustering and cosmic variance.

We report here the results of a search for $z \approx 10$ galaxies in a new set of *JWST* imaging data, obtained by three different programs (GLASS-JWST, UNCOVER, and DDT#2756) in the region of the cluster Abell 2744. The combination of depth (GLASS-JWST is among the deepest fields obtained so far with *JWST*) and lensing magnification (although we limit our analysis to $\mu < 5$, where the lens model is robust) allows us to select with high reliability galaxies down to an intrinsic rest-frame luminosity of $M_{\text{UV}} \approx -19$ mag. Remarkably, we identify 7 galaxies at this redshift, including two previously reported in the first epoch of the GLASS-JWST dataset. Five of the galaxies are detected in the (relatively small) GLASS-JWST area, and are distributed along a filament-like structure ~ 2 Mpc in projected length. This sample consists of an excellent set of candidates for efficient spectroscopic follow-up observations with NIRSpec.

Building upon a revised lensing model that improves the description of the entire A2744 area, by taking advantage of new multiple images and MUSE spectra, we compute the resulting number density in three magnitude bins, and compare it with the results from recent *JWST* surveys. We conclude that the density of bright $z \approx 10$ galaxies in the A2744 region is significantly higher than the average, by factors that range between $3\times$ and $10\times$ depending on M_{UV} and on the survey taken as reference.

We conclude that extending the search on a larger area northwest of the cluster is necessary to further characterize this potential overdensity. Spectroscopic redshifts can determine whether these objects are part of a single physical

³ Following the Cosmic Variance Calculator at <https://www.ph.unimelb.edu.au/~mtrenti/cvc/CosmicVariance.html>. See Trenti & Stiavelli (2008).

overdensity, or the apparent density is enhanced by chance superposition of galaxies at similar redshifts (e.g., [Morishita et al. 2022](#)). Finally, although all candidates show prominent Lyman breaks and robust photometric redshift solutions in the expected range, spectroscopic confirmation is needed to rule out any possible contamination in the sample from rare classes of lower-redshift interlopers ([Vulcani et al. 2017](#); [Zavala et al. 2022](#); [Fujimoto et al. 2022](#)), in particular for objects with limited coverage at short wavelengths.

In conclusion, our study confirms the suprisingly high density of bright galaxies observed in early *JWST* observations but calls for both extensive follow-up spectroscopy and wider surveys along multiple lines of sight to achieve an unbiased estimate of their number density and clustering properties.

This work is based on observations made with the NASA/ESA/CSA *James Webb Space Telescope*. The data were obtained from the Mikulski Archive for Space Telescopes at the Space Telescope Science Institute, which is operated by the Association of Universities for Research in Astronomy, Inc., under NASA contract NAS 5-03127 for *JWST*. These observations are associated with program JWST-ERS-1324. The *JWST* data used in this paper can be found on MAST: <http://dx.doi.org/10.17909/fqaq-p393>. We acknowledge financial support from NASA through grants JWST-ERS-1342. K.G. and T.N. acknowledges support from Australian Research Council Laureate Fellowship FL180100060. C.M. acknowledges support by the VILLUM FONDEN under grant 37459. The Cosmic Dawn Center (DAWN) is funded by the Danish National Research Foundation under grant DNRF140. We acknowledge support from INAF Minigrant “Reionization and fundamental cosmology with high-redshift galaxies” and grants PRIN-MIUR 2017WSCC32, 2020SKSTHZ. A.V.F. received financial assistance from the Christopher R. Redlich Fund and numerous individual donors.

Software: A-PHOT ([Merlin et al. 2019](#)), Astropy ([Astropy Collaboration et al. 2013](#)), EAzY ([Brammer et al. 2008](#)), Matplotlib ([Hunter 2007](#)), SExtractor (v2.8.6 [Bertin & Arnouts 1996](#); [Guo et al. 2013](#)), SCAMP ([Bertin 2006](#)), SWARP ([Bertin et al. 2002](#)), zphot ([Fontana et al. 2000](#))

REFERENCES

- Astropy Collaboration, Robitaille, T. P., Tollerud, E. J., et al. 2013, *A&A*, 558, A33, doi: [10.1051/0004-6361/201322068](https://doi.org/10.1051/0004-6361/201322068)
- Bagley, M. B., Finkelstein, S. L., Rojas-Ruiz, S., et al. 2022, arXiv e-prints, arXiv:2205.12980. <https://arxiv.org/abs/2205.12980>
- Bakx, T. J. L. C., Zavala, J. A., Mitsuhashi, I., et al. 2022, arXiv e-prints, arXiv:2208.13642. <https://arxiv.org/abs/2208.13642>
- Bergamini, P., Acebron, A., Grillo, C., et al. 2022, arXiv e-prints, arXiv:2207.09416. <https://arxiv.org/abs/2207.09416>
- Bertin, E. 2006, in *Astronomical Society of the Pacific Conference Series*, Vol. 351, *Astronomical Data Analysis Software and Systems XV*, ed. C. Gabriel, C. Arviset, D. Ponz, & S. Enrique, 112
- Bertin, E., & Arnouts, S. 1996, *A&AS*, 117, 393
- Bertin, E., Mellier, Y., Radovich, M., et al. 2002, in *Astronomical Society of the Pacific Conference Series*, Vol. 281, *Astronomical Data Analysis Software and Systems XI*, ed. D. A. Bohlender, D. Durand, & T. H. Handley, 228
- Bezanson, R., Labbe, I., Whitaker, K. E., et al. 2022, arXiv e-prints, arXiv:2212.04026. <https://arxiv.org/abs/2212.04026>
- Bouwens, R. J., Illingworth, G. D., van Dokkum, P. G., et al. 2022a, *ApJ*, 927, 81, doi: [10.3847/1538-4357/ac4791](https://doi.org/10.3847/1538-4357/ac4791)
- Bouwens, R. J., Oesch, P. A., Stefanon, M., et al. 2021, *AJ*, 162, 47, doi: [10.3847/1538-3881/abf83e](https://doi.org/10.3847/1538-3881/abf83e)
- Bouwens, R. J., Stefanon, M., Brammer, G., et al. 2022b, arXiv e-prints, arXiv:2211.02607. <https://arxiv.org/abs/2211.02607>
- Bowler, R. A. A., Jarvis, M. J., Dunlop, J. S., et al. 2020, *MNRAS*, 493, 2059, doi: [10.1093/mnras/staa313](https://doi.org/10.1093/mnras/staa313)
- Boylan-Kolchin, M. 2022, arXiv e-prints, arXiv:2208.01611. <https://arxiv.org/abs/2208.01611>
- Brammer, G. 2022, gbrammer/golfir: Software pipeline for model photometry on images with different point spread functions, 1.0, Zenodo, Zenodo, doi: [10.5281/zenodo.7149516](https://doi.org/10.5281/zenodo.7149516)
- Brammer, G. B., van Dokkum, P. G., & Coppi, P. 2008, *ApJ*, 686, 1503, doi: [10.1086/591786](https://doi.org/10.1086/591786)
- Bruzual, G., & Charlot, S. 2003, *MNRAS*, 344, 1000, doi: [10.1046/j.1365-8711.2003.06897.x](https://doi.org/10.1046/j.1365-8711.2003.06897.x)
- Calzetti, D., Armus, L., Bohlin, R. C., et al. 2000, *ApJ*, 533, 682, doi: [10.1086/308692](https://doi.org/10.1086/308692)

- Castellano, M., Fontana, A., Grazian, A., et al. 2012, *A&A*, 540, A39, doi: [10.1051/0004-6361/201118050](https://doi.org/10.1051/0004-6361/201118050)
- Castellano, M., Sommariva, V., Fontana, A., et al. 2014, *A&A*, 566, A19, doi: [10.1051/0004-6361/201322704](https://doi.org/10.1051/0004-6361/201322704)
- Castellano, M., Yue, B., Ferrara, A., et al. 2016, *ApJL*, 823, L40, doi: [10.3847/2041-8205/823/2/L40](https://doi.org/10.3847/2041-8205/823/2/L40)
- Castellano, M., Pentericci, L., Vanzella, E., et al. 2018, *ApJL*, 863, L3, doi: [10.3847/2041-8213/aad59b](https://doi.org/10.3847/2041-8213/aad59b)
- Castellano, M., Fontana, A., Treu, T., et al. 2022a, *ApJL*, 938, L15, doi: [10.3847/2041-8213/ac94d0](https://doi.org/10.3847/2041-8213/ac94d0)
- Castellano, M., Pentericci, L., Cupani, G., et al. 2022b, *A&A*, 662, A115, doi: [10.1051/0004-6361/202243348](https://doi.org/10.1051/0004-6361/202243348)
- Chabrier, G. 2003, *PASP*, 115, 763, doi: [10.1086/376392](https://doi.org/10.1086/376392)
- Dayal, P., & Ferrara, A. 2018, *PhR*, 780, 1, doi: [10.1016/j.physrep.2018.10.002](https://doi.org/10.1016/j.physrep.2018.10.002)
- Donnan, C. T., McLeod, D. J., Dunlop, J. S., et al. 2022, arXiv e-prints, arXiv:2207.12356. <https://arxiv.org/abs/2207.12356>
- Endsley, R., Behroozi, P., Stark, D. P., et al. 2020, *MNRAS*, 493, 1178, doi: [10.1093/mnras/staa324](https://doi.org/10.1093/mnras/staa324)
- Ferrara, A., Pallottini, A., & Dayal, P. 2022, arXiv e-prints, arXiv:2208.00720. <https://arxiv.org/abs/2208.00720>
- Finkelstein, S. L., Ryan, Jr., R. E., Papovich, C., et al. 2015, *ApJ*, 810, 71, doi: [10.1088/0004-637X/810/1/71](https://doi.org/10.1088/0004-637X/810/1/71)
- Finkelstein, S. L., Bagley, M. B., Arrabal Haro, P., et al. 2022a, arXiv e-prints, arXiv:2207.12474. <https://arxiv.org/abs/2207.12474>
- Finkelstein, S. L., Bagley, M. B., Ferguson, H. C., et al. 2022b, arXiv e-prints, arXiv:2211.05792. <https://arxiv.org/abs/2211.05792>
- Finkelstein, S. L., Bagley, M., Song, M., et al. 2022c, *ApJ*, 928, 52, doi: [10.3847/1538-4357/ac3aed](https://doi.org/10.3847/1538-4357/ac3aed)
- Fiore, F., Ferrara, A., Bischetti, M., Feruglio, C., & Travascio, A. 2022, arXiv e-prints, arXiv:2211.08937. <https://arxiv.org/abs/2211.08937>
- Fontana, A., D’Odorico, S., Poli, F., et al. 2000, *AJ*, 120, 2206, doi: [10.1086/316803](https://doi.org/10.1086/316803)
- Fontana, A., Dunlop, J. S., Paris, D., et al. 2014, *A&A*, 570, A11, doi: [10.1051/0004-6361/201423543](https://doi.org/10.1051/0004-6361/201423543)
- Fujimoto, S., Finkelstein, S. L., Burgarella, D., et al. 2022, arXiv e-prints, arXiv:2211.03896. <https://arxiv.org/abs/2211.03896>
- Furtak, L. J., Zitrin, A., Weaver, J. R., et al. 2022, arXiv e-prints, arXiv:2212.04381. <https://arxiv.org/abs/2212.04381>
- Gehrels, N. 1986, *ApJ*, 303, 336, doi: [10.1086/164079](https://doi.org/10.1086/164079)
- Grazian, A., Castellano, M., Fontana, A., et al. 2012, *A&A*, 547, A51, doi: [10.1051/0004-6361/201219669](https://doi.org/10.1051/0004-6361/201219669)
- Guo, Y., Ferguson, H. C., Giavalisco, M., et al. 2013, *ApJS*, 207, 24, doi: [10.1088/0067-0049/207/2/24](https://doi.org/10.1088/0067-0049/207/2/24)
- Harikane, Y., Ouchi, M., Oguri, M., et al. 2022, arXiv e-prints, arXiv:2208.01612. <https://arxiv.org/abs/2208.01612>
- Hunter, J. D. 2007, *Computing in Science and Engineering*, 9, 90, doi: [10.1109/MCSE.2007.55](https://doi.org/10.1109/MCSE.2007.55)
- Kannan, R., Springel, V., Hernquist, L., et al. 2022, arXiv e-prints, arXiv:2210.10066. <https://arxiv.org/abs/2210.10066>
- Kawamata, R., Ishigaki, M., Shimasaku, K., et al. 2018, *ApJ*, 855, 4, doi: [10.3847/1538-4357/aaa6cf](https://doi.org/10.3847/1538-4357/aaa6cf)
- Kohandel, M., Ferrara, A., Pallottini, A., et al. 2022, arXiv e-prints, arXiv:2212.02519. <https://arxiv.org/abs/2212.02519>
- Kron, R. G. 1980, *ApJS*, 43, 305, doi: [10.1086/190669](https://doi.org/10.1086/190669)
- Larson, R. L., Hutchison, T. A., Bagley, M., et al. 2022, arXiv e-prints, arXiv:2211.10035. <https://arxiv.org/abs/2211.10035>
- Leethochawalit, N., Roberts-Borsani, G., Morishita, T., Trenti, M., & Treu, T. 2022a, arXiv e-prints, arXiv:2205.15388. <https://arxiv.org/abs/2205.15388>
- Leethochawalit, N., Trenti, M., Santini, P., et al. 2022b, arXiv e-prints, arXiv:2207.11135. <https://arxiv.org/abs/2207.11135>
- Mason, C. A., Trenti, M., & Treu, T. 2022, arXiv e-prints, arXiv:2207.14808. <https://arxiv.org/abs/2207.14808>
- McLeod, D. J., McLure, R. J., & Dunlop, J. S. 2016, *MNRAS*, 459, 3812, doi: [10.1093/mnras/stw904](https://doi.org/10.1093/mnras/stw904)
- Melia, F. 2014, *AJ*, 147, 120, doi: [10.1088/0004-6256/147/5/120](https://doi.org/10.1088/0004-6256/147/5/120)
- Menci, N., Castellano, M., Santini, P., et al. 2022, *ApJL*, 938, L5, doi: [10.3847/2041-8213/ac96e9](https://doi.org/10.3847/2041-8213/ac96e9)
- Merlin, E., Fortuni, F., Torelli, M., et al. 2019, *MNRAS*, 490, 3309, doi: [10.1093/mnras/stz2615](https://doi.org/10.1093/mnras/stz2615)
- Merlin, E., Bonchi, A., Paris, D., et al. 2022, arXiv e-prints, arXiv:2207.11701. <https://arxiv.org/abs/2207.11701>
- Merten, J., Coe, D., Dupke, R., et al. 2011, *MNRAS*, 417, 333, doi: [10.1111/j.1365-2966.2011.19266.x](https://doi.org/10.1111/j.1365-2966.2011.19266.x)
- Morishita, T., & Stiavelli, M. 2022, arXiv e-prints, arXiv:2207.11671. <https://arxiv.org/abs/2207.11671>
- Morishita, T., Trenti, M., Stiavelli, M., et al. 2018, *ApJ*, 867, 150, doi: [10.3847/1538-4357/aae68c](https://doi.org/10.3847/1538-4357/aae68c)
- Morishita, T., Roberts-Borsani, G., Treu, T., et al. 2022, arXiv e-prints, arXiv:2211.09097. <https://arxiv.org/abs/2211.09097>
- Naidu, R. P., Oesch, P. A., van Dokkum, P., et al. 2022, arXiv e-prints, arXiv:2207.09434. <https://arxiv.org/abs/2207.09434>
- Oesch, P. A., Bouwens, R. J., Illingworth, G. D., Labbé, I., & Stefanon, M. 2018, *ApJ*, 855, 105, doi: [10.3847/1538-4357/aab03f](https://doi.org/10.3847/1538-4357/aab03f)
- Oke, J. B., & Gunn, J. E. 1983, *ApJ*, 266, 713, doi: [10.1086/160817](https://doi.org/10.1086/160817)
- Pontoppidan, K. M., Barrientes, J., Blome, C., et al. 2022, *ApJL*, 936, L14, doi: [10.3847/2041-8213/ac8a4e](https://doi.org/10.3847/2041-8213/ac8a4e)
- Prieto-Lyon, G., Strait, V., Mason, C. A., et al. 2022, arXiv e-prints, arXiv:2211.12548. <https://arxiv.org/abs/2211.12548>
- Roberts-Borsani, G., Morishita, T., Treu, T., Leethochawalit, N., & Trenti, M. 2022a, *ApJ*, 927, 236, doi: [10.3847/1538-4357/ac4803](https://doi.org/10.3847/1538-4357/ac4803)
- Roberts-Borsani, G., Treu, T., Chen, W., et al. 2022b, arXiv e-prints, arXiv:2210.15639. <https://arxiv.org/abs/2210.15639>

- Robertson, B. E. 2022, *ARA&A*, 60, 121, doi: [10.1146/annurev-astro-120221-044656](https://doi.org/10.1146/annurev-astro-120221-044656)
- Robertson, B. E., Tacchella, S., Johnson, B. D., et al. 2022, arXiv e-prints, arXiv:2212.04480. <https://arxiv.org/abs/2212.04480>
- Salpeter, E. E. 1955, *ApJ*, 121, 161, doi: [10.1086/145971](https://doi.org/10.1086/145971)
- Santini, P., Fontana, A., Castellano, M., et al. 2022, arXiv e-prints, arXiv:2207.11379. <https://arxiv.org/abs/2207.11379>
- Schaerer, D., & de Barros, S. 2009, *A&A*, 502, 423, doi: [10.1051/0004-6361/200911781](https://doi.org/10.1051/0004-6361/200911781)
- Sersic, J. L. 1968, *Atlas de galaxias australes* (Cordoba, Argentina: Observatorio Astronomico, 1968)
- Steinhardt, C. L., Jauzac, M., Acebron, A., et al. 2020, *ApJS*, 247, 64, doi: [10.3847/1538-4365/ab75ed](https://doi.org/10.3847/1538-4365/ab75ed)
- Trenti, M., & Stiavelli, M. 2008, *ApJ*, 676, 767, doi: [10.1086/528674](https://doi.org/10.1086/528674)
- Treu, T., Roberts-Borsani, G., Bradac, M., et al. 2022, *The Astrophysical Journal*, 935, 110, doi: [10.3847/1538-4357/ac8158](https://doi.org/10.3847/1538-4357/ac8158)
- Treu, T., Calabro, A., Castellano, M., et al. 2022, arXiv e-prints, arXiv:2207.13527. <https://arxiv.org/abs/2207.13527>
- Vulcani, B., Trenti, M., Calvi, V., et al. 2017, *ApJ*, 836, 239, doi: [10.3847/1538-4357/aa5caf](https://doi.org/10.3847/1538-4357/aa5caf)
- Yan, H., Cohen, S. H., Windhorst, R. A., et al. 2022, arXiv e-prints, arXiv:2209.04092. <https://arxiv.org/abs/2209.04092>
- Yang, L., Leethochawalit, N., Treu, T., et al. 2022, *MNRAS*, 514, 1148, doi: [10.1093/mnras/stac1236](https://doi.org/10.1093/mnras/stac1236)
- Yoon, I., Carilli, C. L., Fujimoto, S., et al. 2022, arXiv e-prints, arXiv:2210.08413. <https://arxiv.org/abs/2210.08413>
- Zavala, J. A., Buat, V., Casey, C. M., et al. 2022, arXiv e-prints, arXiv:2208.01816. <https://arxiv.org/abs/2208.01816>
- Ziparo, F., Ferrara, A., Sommovigo, L., & Kohandel, M. 2022, arXiv e-prints, arXiv:2209.06840. <https://arxiv.org/abs/2209.06840>
- Zitrin, A., Zheng, W., Broadhurst, T., et al. 2014, *ApJL*, 793, L12, doi: [10.1088/2041-8205/793/1/L12](https://doi.org/10.1088/2041-8205/793/1/L12)